

# The onion universe: all sky lightcone simulations in spherical shells

Pablo Fosalba, Enrique Gaztañaga, Francisco J Castander & Marc Manera

*Institut de Ciències de l'Espai, IEEC-CSIC, Campus UAB, F. de Ciències, Torre C5 par-2, Barcelona 08193, Spain*

4 September 2008

## ABSTRACT

Galaxy surveys provide a large-scale view of the universe that typically has a limited line-of-sight or redshift resolution. The lack of radial accuracy in these surveys can be modelled by picturing the universe as a set of concentric radial shells of finite width around the observer, i.e. an onion-like structure. We present a new N-body simulation with  $2048^3$  particles developed at the Marenostrum supercomputer with the GADGET-2 code. Using the lightcone output we build a set of angular maps that mimic this onion-like representation of the universe. The onion maps are a highly compressed version of the raw data (i.e., a factor  $> 1000$  smaller size for arcminute resolution maps) and they provide a new and powerful tool to exploit large scale structure observations. We introduce two basic applications of these maps that are especially useful for constraining dark energy properties: the baryon acoustic oscillations (BAO) in the galaxy power spectrum and all-sky maps of the weak lensing distortion. In particular, from the matter density maps, we determine the smallest scale where linear theory and the Gaussianity of the error analysis applies. Using the weak lensing maps, we measure the convergence power spectra and compare it to halo fit predictions. We also discuss mass resolution effects and error determinations. As a further application, we compute the variance and higher-order moments of the maps. We show that sampling variance on scales of few degrees is quite large, resulting in a significant (25% at 10 arcminute scales) bias in the variance. We caution that current lensing surveys such as the COSMOS HST should take into account this bias and extra sampling error in their clustering analyses and inferred cosmological parameter constraints. Finally, we test the importance of projection effects in the weak lensing mass reconstruction. On the mean, the mass calibration works well but it exhibits a large non-Gaussian scatter what could induce a large bias in the recovered mass function.

## 1 INTRODUCTION

Upcoming astronomical surveys will gather many Terabytes of unprecedented high quality data containing the relevant information to answer key cosmological questions, ranging from the nature of the initial conditions in the structure formation of the universe, how galaxies and clusters form and evolve, or the properties of the so called dark energy and theory of gravity on cosmological scales.

These datasets will pose a great challenge to the scientific community to develop the appropriate data analysis tools to compress the overwhelming raw data into a few numbers, eg a set of cosmological parameters. Simulating surveys, with their anticipated volume, resolution and complexity, has become a standard tool to prepare the scien-

tific exploitation and to understand real astronomical data. Thus, analyzing mock surveys suffers from similar limitations, with the agravant that it requires a large number of simulations to pin down statistical errors and explore cosmological parameter space.

Measuring redshifts for many galaxies is very costly (especially at  $z > 1$ ), even for very large telescopes. Thus, to explore the largest scales with catalogs containing many millions of galaxies typically requires a photometric approach to obtain galaxy redshifts, as is the case for most of the upcoming or planned surveys (such as DES, PAU, VHS, PanSTARRS, LSST, DUNE). In these surveys information in the radial direction is washed out on scales smaller than

the photometric error width. This limits the amount of information that can be used for scientific analysis.

With this motivation, in this paper we develop a new approach to building mock surveys, that we dub the “onion universe”, which mimics the tomographic structure of photometric surveys by decomposing the full 3D lightcone data structure into a set of concentric 2D all-sky maps around the observer. We thus propose this method as a new and efficient tool to exploit upcoming large photometric surveys. In particular, this new approach allows us to make the following main contributions that we present in this paper:

- *Data Compression*: for most of its cosmological applications, our approach provides an effectively lossless method to compress simulated data by a factor  $\sim 1000$  for arcminute resolution angular maps. This allows Terabyte-sized simulations containing tens of billions of particles to be analyzed in a regular laptop.
- *BAOs in the angular power spectrum*: using the set of dark-matter density shells resulting from our decomposition of the N-body lightcone data, we can straightforwardly study the BAOs in the angular clustering of dark-matter. As an application of this, we assess the limit of applicability of linear theory (and Gaussianity of the error) as a function of redshift from an angular power spectrum analysis.
- *All-sky weak lensing maps*: our method provides a straightforward way to simulate all-sky maps of tracers of the large-scale structure in the light-cone from weighted combinations of 2D density maps. The main application of the “onion universe” method presented in this paper is the development, for the first time, of an adequate all-sky simulated weak lensing map with fine angular resolution. Our map is validated through a comparison with theoretical predictions for the power spectrum over 3 decades in angular scales. We use this mock map to investigate effects of sampling bias in current weak lensing surveys from higher-order moments of the convergence field, and discuss the potential and limitations of using weak lensing as a cluster mass calibrator.

Weak gravitational lensing by the large-scale structure of the universe probes density fluctuations in a wide dynamical range, from linear to highly non-linear scales. Current lensing observations (eg Bacon et al. 2001; Refregier et al 2002; Jarvis et al. 2006; Massey et al 2007) can only sample the smaller scales (ie smaller than a degree) which are dominated by non-linear fluctuations. Since there is no accurate analytic description of the dark matter density field in the non-linear regime it is thus necessary to resort to numerical simulations to make accurate predictions of the weak lensing distortions.

Simulations of weak gravitational lensing are based on implementations of the ray tracing technique on N-body simulations (eg see Wambsganss et al 2000; Jain et al 2000; Vale & White 2003, and references therein). In this approach light rays are propagated from the observer to the

source by computing the distortion and magnification effects from multiple (from tens to a hundred) of equally spaced projected-mass lens planes. This approach has proven to be successful in measuring the lensing power spectrum which was found to be in agreement with the Born and Limber approximations (eg Jain et al 2000; Vale & White 2003). In addition, the lensing higher order moments induced by density fluctuations in the non-linear regime can also be estimated (eg Jain et al 2000; White & Hu 2000; Vale & White 2003; White & Vale 2004) and they turn out to be consistent with perturbation theory results on the largest scales and analytic fits on intermediate scales (eg Gaztañaga & Bernardeau 1998; Waerbeke et al 2000). In particular, measurements of the variance and skewness of the lensing maps can be used to constrain the amplitude of matter fluctuations,  $\sigma_8$ , and matter density,  $\Omega_m$  (Bernardeau, van Waerbeke & Mellier 1997; Jain & Seljak 1997).

However, covering a wide enough dynamical range (from Mpc to Gpc scales) is prohibitive with current implementations of ray tracing techniques and therefore simulations so far have focused on small patches of the sky (i.e few square degrees), comparable to the areas covered by current surveys (such as GEMS, COSMOS HST, CFHTLS), well in the non-linear regime, where most of the lensing signal is expected to come from. Moreover, as we will show below, statistical measurements in small volume simulated surveys may be significantly affected by sampling bias (Hui & Gaztañaga 1999) and cosmic variance errors are largely enhanced by non-Gaussianity (Scoccimarro et al 1999; Semboloni et al 2007). For a review on the weak lensing formalism, simulations and observations see Bartelmann & Schneider (2001), Refregier (2003) and references therein.

Previous work on simulating observational data in terms of lightcone surveys has concentrated on galaxy mocks (see e.g. Blaizot et al 2005; Kitzbichler & White 2007; Forero-Romero et al 2007 and references therein), where finite simulation volume, redshift discreteness, and cosmic variance were carefully addressed.

This paper is organized as follows: Section 2 presents the simulations, the onion maps and its power spectrum. In Section 3, we introduce the new method to build the weak lensing maps from the onion shells and present several tests to validate the method. We also discuss different error estimates based on the convergence maps and a comparison with the halo-fit prediction. Section 4 is devoted to the study of non-Gaussianity, mass reconstruction and mass function. Finally, in Section 5 we summarize our main results and conclusions.

## 2 ONION MAPS

We have developed a set of large N-body simulations with Gadget-2 (Springel 2005) on the Marenostrum supercom-

**Table 1.** MICE N-body simulations used in this paper.

$L_{box}$ Mpc/h	$N_{par}$ number	particle mass $10^{10} M_{sun}/h$
3072	512 <sup>3</sup>	1510
3072	1024 <sup>3</sup>	190
3072	2048 <sup>3</sup>	24

puter at BSC<sup>1</sup>. We shall name them MICE (MareNostrum - Instituto de Ciencias del Espacio) simulations hereafter<sup>2</sup>. In this paper we focus on a simulation run with 2048<sup>3</sup> dark-matter particles in a box-size of  $L_{box} = 3072$  Mpc/h, and assume a flat concordance  $\Lambda$ CDM model with  $\Omega_m = 0.25$ ,  $\Omega_\Lambda = 0.75$ ,  $\Omega_b = 0.044$ ,  $n_s = 0.95$ ,  $\sigma_8 = 0.8$  and  $h = 0.7$ . The resulting particle mass is  $M = 2.34 \times 10^{11} M_{sun}/h$  and the softening length used is 50 Kpc/h. Thus our simulation has a dynamic range close to five orders of magnitude. We start our run at  $z_i = 50$  displacing particles using the Zel-dovich dynamics. The MICE simulation has a similar number of particles to the Millenium simulation (Springel et al 2005) but  $6^3 = 216$  times more volume (and corresponding larger particle mass). This makes the MICE simulation more adequate than the Millenium for very large scale statistical analyses, such as the search of the baryon acoustic scale (see below) and the study of very long distance effects (such as gravitational lensing). The drawback is the limited resolution that is required to study smaller scales and substructure in galaxy size halos. In terms of volume, our simulation is similar to the Hubble Volume (Evrard et al 2002), but it has 8 times better mass resolution. Given that we have a relatively large particle mass, we have also used some MICE runs with different number of particles, given in Table 1, to test resolution effects. We have also varied the box size, ranging from  $L_{box} = 768$  Mpc/h to  $L_{box} = 7680$  Mpc/h, to explore volume effects. Results from this analysis will be discussed in detail elsewhere.

We have built a lightcone output of this simulation from  $\sim 200$  comoving outputs which are separated by constant spacing in cosmic time ( $\approx 70$  Myr). The lightcone has been constructed in spherical concentric shells, each one getting its particles from one of the comoving outputs. The distance from the center of the set of spherical shells, where the observer is, to the mean radial distance of each shell is given by the corresponding redshift of each comoving output. In every shell the dark matter particles are moved using their peculiar velocities in order to extrapolate them into their lightcone positions. We have allowed a spherical shell buffer

to take into account the particles that cross shell boundaries when moved.

The lightcone extends out to  $z_{LC} \simeq 6$  (i.e., a comoving distance  $r_{LC} \simeq 6$  Gpc/h from the observer) by replicating twice the parent simulation with  $L_{box}$  size along each cartesian direction and applying periodic boundary conditions. Note that a radial comoving distance of 3 Gpc/h corresponds to  $z \simeq 1.4$ , where cosmic evolution plays a significant role for an observer at  $z = 0$ , so we do not expect this periodic repetition to have much impact on our analysis. We plan to explore this issue further in future work by comparing results of different  $L_{box}$ . Preliminary results indicate that  $L_{box} = 3072$  Mpc/h is large enough for most applications we have explored.

We have done several tests with the simulation output to make sure that basic clustering statistics, such as the power spectrum, the halo mass function and the higher order correlations, are consistent with previous results. As shown below, we have measured the baryon acoustic oscillations (BAO) imprinted in the matter distribution at different redshifts or onion shells and found good agreement with other analyses. More details will be presented elsewhere.

## 2.1 Redshift shells and BAO

We discretize the lightcone output of the simulation in concentric spherical shells of width  $dz$  given by a constant spacing in cosmic time. We use a spacing of  $\approx 70$  Myr to match the width used for the shells in the lightcone construction described above. This corresponds to a  $dz$  that varies from  $dz \simeq 0.005$  at low  $z$  to  $dz \simeq 0.025$  at  $z = 1.4$  (which corresponds to a width of  $\simeq 16$  Mpc/h to 35 Mpc/h). This is probably enough for most large scale applications. Each onion shell is stored as a number density pixel map of given resolution in the Healpix format (Górski et al 1998). Here we use maps with  $N_{side} = 2048$ , which pixelizes the sky with  $12N_{side}^2 \approx 50$  million cells of size  $\theta_{pix} \simeq 1.7$  arcmin size. The resulting onion universe decomposition of the parent simulation is shown in Fig.1.

Fig.2-5 show four spherical shells of the onion universe corresponding to the projected matter density distribution for four different redshifts (with brighter colours representing higher number of particles per pixel in a log scale). It is clearly visible a characteristic  $\sim 100$  Mpc/h cell of filamentary structure (the so-call Cosmic Web, ie Bond et al 1996). The cell-size shrinks to smaller angular scales and smaller particle number density contrast as we move to larger redshifts. By  $z = 0.6$ , there are already close to a thousand of these 100 Mpc/h cells in this single onion shell (i.e., Fig.5). It is precisely around this  $\simeq 100$  Mpc/h scale that future surveys will aim at measuring the baryon acoustic oscillations scale,  $r_{BAO}$ . The relative error involved in measuring  $r_{BAO}$  is roughly proportional to the inverse of the square

<sup>1</sup> Barcelona Supercomputing Center, [www.bsc.es](http://www.bsc.es)

<sup>2</sup> Projected matter density and weak lensing maps from the MICE simulations are publicly available at <http://www.ice.cat/mice>

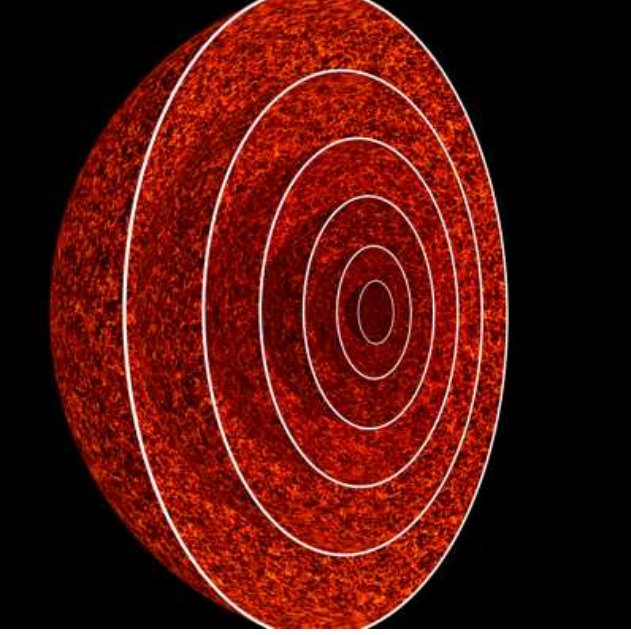


**Figure 1.** The onion universe: a decomposition of the lightcone that mimics the data structure in photometric galaxy surveys. The simulated universe is rendered as a discrete set of projected matter density spherical shells in the lightcone around the observer, i.e. at the center of the concentric spheres. 2D spherical shells are equally spaced in comoving time and pixelized using the Healpix tessellation of chosen angular resolution. For clarity, in this figure we only show one of the hemispheres (i.e half the onion universe) for several of the lowest redshift shells.

root of the number of independent  $r_{BAO}$  cells:

$$\Delta_{BAO} \equiv \frac{\Delta r_{BAO}}{r_{BAO}} \simeq \left( \frac{r_{BAO}^3}{V} \right)^{1/2} \quad (1)$$

where  $V$  is the sampled volume, and we have assumed Gaussian errors (with negligible shot-noise) over the first two BAO wiggles (see also Angulo et al 2008). Thus, for the onion shell at  $z = 0.6$  we estimate  $\Delta_{BAO} \simeq 1/\sqrt{1000} \simeq 3\%$ . According to this rule of thumb, we can get to 0.6% relative error in measuring  $r_{BAO}$  using the whole MICE simulation volume, as compared to 9% with the Millenium simulation.

## 2.2 Compression factor

To build the light-cone with sufficient accuracy, we have used 200 comoving simulation outputs. Each output takes 250 Gbytes, so the total storage required is about 49 Terabytes. If we match the spatial width of the onion shells (as we have done) to the time lag between the outputs that are used to build the light-cone we will have equivalent information for applications that do not require angular or redshift resolution better than that projected onto the pixel maps. We have produced 200 such Healpix maps, each occupies 201 Megabyte, which represents a total of 39 Gigabytes. Thus, there is total compression factor of about 1300 when using

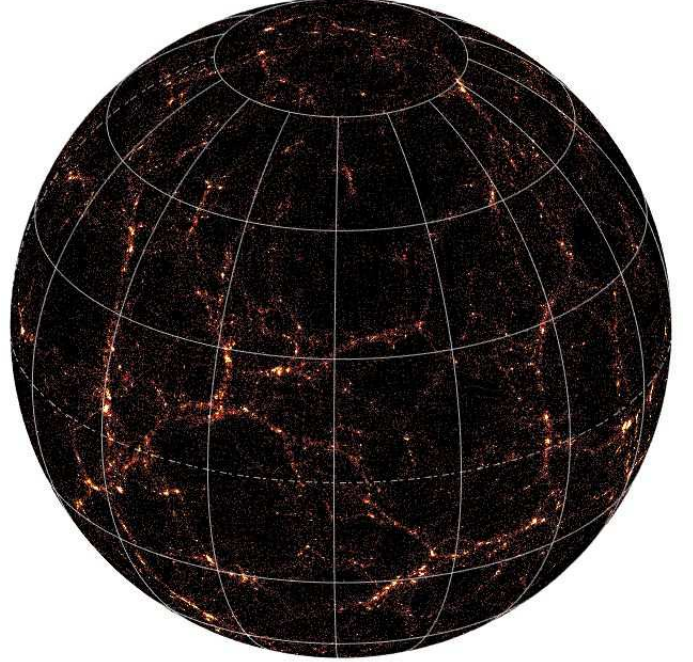


**Figure 2.** Onion shell density map at  $z \simeq 0.036$  (this corresponds to a comoving distance of  $r = 108 \pm 8$  Mpc/h)

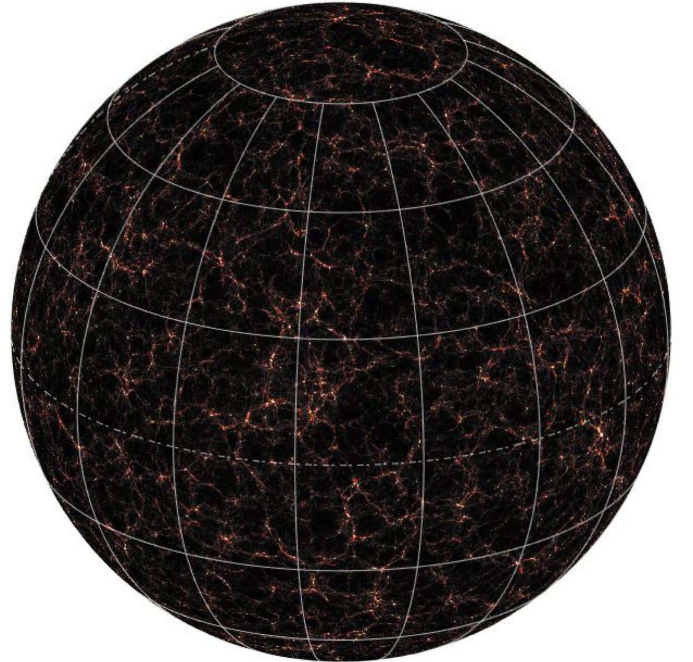


**Figure 3.** Onion shell density map at  $z \simeq 0.15$  (comoving distance  $r = 439 \pm 9$  Mpc/h)



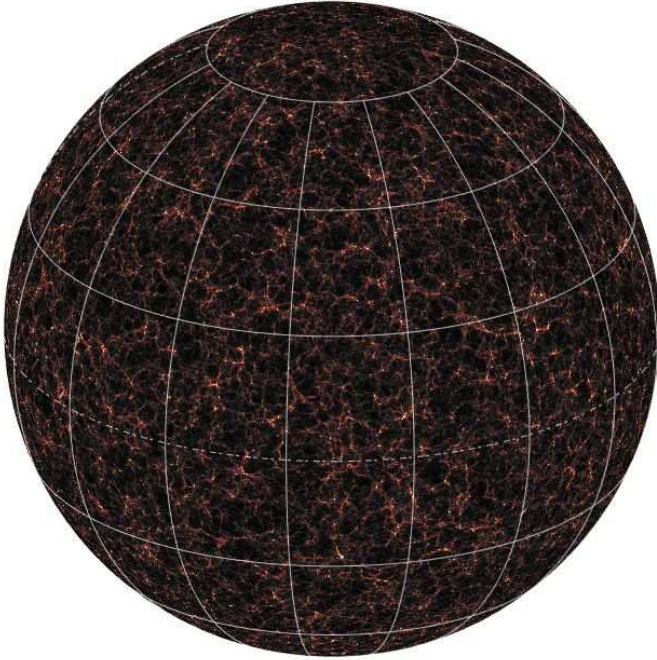


**Figure 4.** Onion shell density map at  $z \simeq 0.30$  (comoving distance  $r = 866 \pm 10$  Mpc/h)

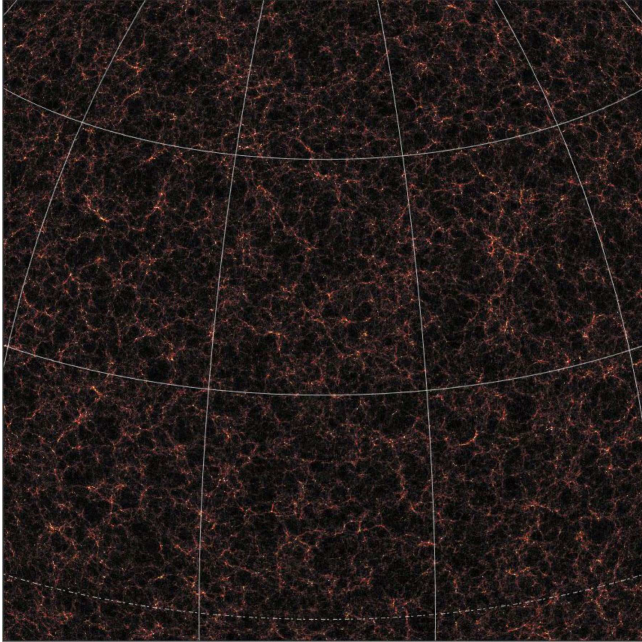


**Figure 5.** Zoom over a shell at  $z \simeq 0.60$  (comoving distance  $r = 1589 \pm 12$  Mpc/h).

the pixel maps instead of the full comoving outputs. Nowadays, it is practically impossible to manage and share 49 Terabytes of data in a public network: it will take more than a year to transfer these data over a 10 Mbit/sec connection. On the other hand, 39 Gbytes fits into a laptop and can be shared in a matter of hours. There are applications for which we might need the full MICE output information, but in many cases the pixel maps will be very useful, specially when we compare to observations in photometric surveys, as we show next.

### 2.3 Angular Power spectrum

Fig.6 shows the total power per log multipole interval  $P_l \equiv l(l+1) C_l/2\pi$  measured from the all-sky onion maps. We have combined thin onion maps into  $dz = 0.1$  slices to match the photo- $z$  error expected for a survey such as the photometric SDSS (Adelman-McCarthy et al 2006) or DES (Annis et al 2005)<sup>3</sup>. Symbols in the figure correspond to the  $P_l$  estimation in maps with redshift ranges (from top to bottom):  $z = 0.4 - 0.5$ ,  $0.9 - 1.0$  and  $1.4 - 1.5$ .

As expected, the amplitude of the fluctuations decreases with the depth of the slice. The BAO wiggles (around  $l \simeq 80 - 300$ ), which are clearly visible, also move to smaller angular scales (higher multipoles). The scatter within multipole bins (i.e., the “intra-bin” variance) estimates the sampling variance for band limited measurements (Fosalba & Szapudi 2004), although this method requires appropriate calibration with simulations. In Section 3 we compare a simple implementation of the intra-bin variance against other more standard error estimators. Shot-noise (shown as a dotted line) does not affect the  $C_l$  estimation within the range of scales shown.

Linear theory predictions are shown by the continuous lines. Simulations match well the linear prediction up to scales of around the first BAO wiggle. On smaller scales (larger multipoles) non-linear effects become important. This effect is larger at low redshift, as expected. For the smallest redshift bin shown ( $z = 0.4 - 0.5$ ), there is a flattening of the power on scales  $l > 2000$  indicating the virialization of structures.

Fig.7 highlights the BAOs in the  $C_l$ ’s by normalizing to the linear theory prediction without baryons (i.e., same cosmological parameters but  $\Omega_b = 0$ ). The first prominent step at  $l_h = 10$  corresponds to the horizon scale at the matter-radiation transition. The first BAO is found at around  $l_1 = 80$  for  $z = 0.4 - 0.5$  and  $l_1 = 160$  for  $z = 0.9 - 1.0$ . These multipoles correspond to the projected scale for the first peak in the 3D power spectrum,  $k_1 \simeq l_1/r(z) \simeq 0.07$ , where  $r(z)$

<sup>3</sup> We take the mean depth of the survey to be  $z \simeq 0.7$ , but this has a very small effect over the maps because the selection function is normalized to be unity in each slice

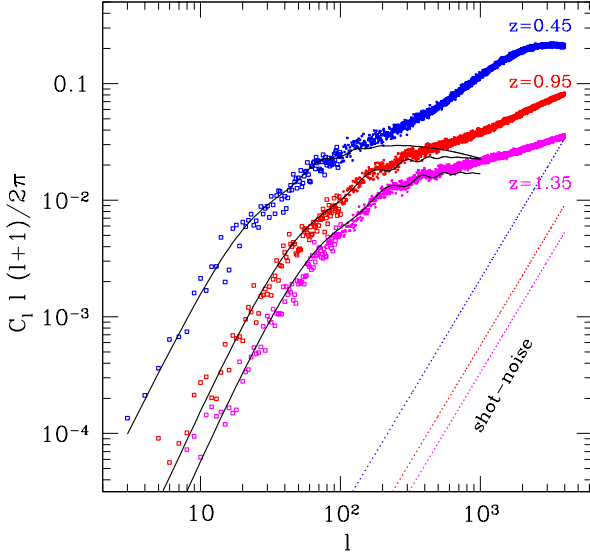


**Figure 6.** Angular power spectrum estimated from combinations of onion maps (symbols) of width  $dz = 0.10$  and mean redshifts of  $z = 0.45$  (top),  $z = 0.95$  (middle) and  $z = 1.35$  (bottom). The continuous line shows the linear theory prediction for each redshift. The dotted line shows the shot-noise contribution in each case.

is the comoving distance to the onion slice and the approximation is valid for small angular scales (i.e., we employ the Limber approximation).

On scales where linear theory is valid and for  $l > 10$  it is usually assumed that the  $C_l$  amplitudes follow a Gaussian distribution with sampling errors given by the Gaussian prediction  $\sigma_G^2 = 2C_l^2/(l+1)$ . We can test this hypothesis with our maps by calculating the Gaussian  $\chi^2$ :

$$\chi^2 = \sum_{l=10}^{l=lm_{\max}} \frac{(C_l^m - C_l^t)^2}{\sigma_G^2} \quad (2)$$

where  $C_l^m$  are the measured values and  $C_l^t$  are the linear theory predictions. We find  $\chi^2 = 281$  and  $\chi^2 = 100$  for  $z = 0.95$  and  $z = 0.45$  respectively. We use  $lm_{\max} = 230$  and  $lm_{\max} = 120$  to include the whole first BAO wiggle. These values are larger than expected for a sum of Gaussian variables for the  $z = 0.95$  case, and are fine for  $z = 0.45$ . The probabilities of this to happen are  $P[\chi^2] = 70\%$  for  $z = 0.45$  and  $P[\chi^2] = 0.26\%$  for  $z = 0.95$ . The later probability increases to  $P[\chi^2] = 12\%$  for  $z = 0.95$  if we use  $lm_{\max} = 177$  (half the way through the first BAO wiggle). This indicates that even on these very large scales and early times there is correlation between different modes and one should be careful when doing precision forecasts using Gaussian errors. The correlation between bins is weaker if we bin the data in multipoles (see below). However, the problem seems more critical at high redshift where the BAO wiggle is bet-

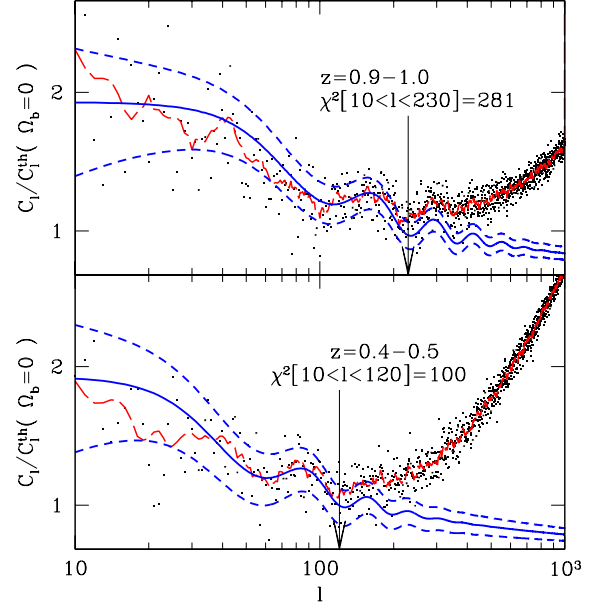


**Figure 7.** Angular power spectrum normalized to a linear model without baryons. The continuous line corresponds to the linear theory prediction (with baryons) while the dashed lines marks the 1-sigma Gaussian errorbars. The dots correspond to measurements in the simulated maps. The long-dashed (red) line just shows a smooth version of the dots.

ter sampled and there are larger projection effects. A more detailed analysis of this effect requires more realizations and will be presented elsewhere.

### 3 CONVERGENCE MAPS

A basic quantity in weak lensing is the convergence field. In the so-called Born approximation, one integrates the lensing distortion over the unperturbed photon paths which is a good approximation for most applications (eg see Cooray & Hu 2000; Bartelmann & Schneider 2001; Vale & White 2003; Refregier 2003). In this approximation, the convergence is just a weighted projected surface density:

$$\kappa(\theta) = \frac{3H_0^2\Omega_m}{2c^2} \int dr \delta(r, \theta) \frac{(r_s - r)r}{r_s a} \quad (3)$$

where  $\delta$  is the 3D matter density at radial distance  $r$  and angular position  $\theta$  (which is here a 2D vector) and  $r_s$  is the radial position of the lensing sources.<sup>4</sup> Out of  $\kappa$  we can get all other quantities of interest such as magnification, demagnification, shear, projected potential or deflection angle (see

<sup>4</sup> Without loss of generality we will assume on writing equations that we live in a flat universe and that all lensing sources are at a fixed redshift  $z_s$ , or radial distance  $r_s$ . It is straightforward to generalize this to an arbitrary distribution of sources, eg (Bartelmann & Schneider 2001; Refregier 2003).



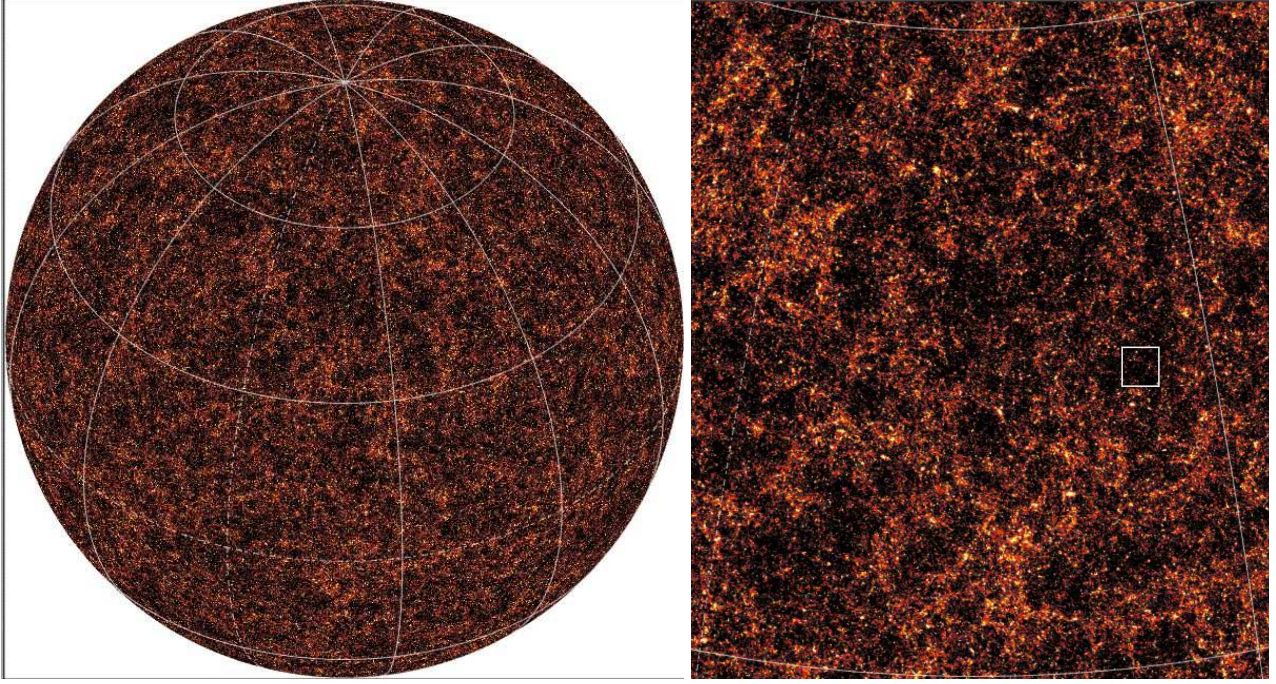


**Figure 8.** Left: All-sky convergence map with sources at  $z_s = 1$ . Right: A  $15 \times 15$  degrees zoom in the central region. The small white square shows an area of  $1.6 \text{ deg}^2$ , comparable to the COSMOS HST survey area.

Bartelmann & Schneider 2001; Refregier 2003 for a review). Some of these relations are not local (they involve derivatives or integrals) but for an all-sky map, all these quantities are trivially related. In harmonic (or 2D Fourier) space, we can transform a convergence map into a gravitational potential or shear map by just multiplying the harmonic (or Fourier)  $\kappa$  amplitudes by the appropriate combination of multipole or wave numbers. However, in the observable universe the boundaries of a real survey complicate these transformations.

We will build our convergence map by just adding the onion slices from the simulation with the appropriate lensing weight. This can be done as follows (see also Gaztañaga & Bernardeau 1998):

$$\kappa(i) = \frac{3H_0^2\Omega_m}{2c^2} \sum_j \delta(i, j) \frac{(r_s - r_j)r_j}{r_s a_j} dr_j \quad (4)$$

where  $i$  indicates a pixel position in the sky and  $j$  a radial bin (at distance  $r_j$  of width  $dr_j$ ) into which we have sliced the simulation as described in the previous section. If we indicate by  $N_{ij}$  the number of particles in pixel  $i$  from onion slice  $j$ , we have:

$$\delta(i, j) = \frac{\rho(i, j)}{\bar{\rho}} - 1 \quad (5)$$

where  $\bar{\rho} = \langle \rho(i, j) \rangle$  and

$$\rho(i, j) = \frac{N_{ij}}{dV_j} = \frac{N_{ij}}{\Delta\Omega r_j^2 dr_j} \quad (6)$$

where  $\Delta\Omega$  is the area of each pixel.

Fig.8 shows images of the resulting maps for lensing sources at  $z_s = 1$ . Note how despite the large volume projected there is still considerable structure in these maps. In particular, on scales of a few square degrees there is a large variation from place to place in the maps. This indicates that sampling variance is important. Current weak lensing surveys, such as COSMOS (Massey et al 2007), or lensing simulations, only expand scales of the order of a few square degrees. Our convergence maps show that sampling variance is quite large on such small scales and it is unlikely that current data could represent a fair sample of the universe. In section 4 and in the Conclusions we will show some more quantitative consequences of this note.

### 3.1 Validation of the map

We can validate the convergence map by comparing its power spectrum and higher orders to theoretical expectations. First we will focus on a comparison with linear theory and a consistency test for the angular power spectrum.

Based on its definition in Eq.3 we would expect the angular power spectrum of the convergence to yield:

$$C_l(\kappa) = \frac{9H_0^4\Omega_m^2}{4c^4} \int dr P(k, z) \frac{(r_s - r)^2}{r_s^2 a^2} \quad (7)$$

where  $P(k, z)$  is the 3D density power spectrum in the simulation at redshift  $z$  (corresponding to the radial coordinate  $r = r(z)$  in the integral) evaluated at  $k = l/r$  in the small

angle (Limber) approximation, valid for  $l > 10$  within a few percent accuracy (see e.g. Vale & White 2003). In terms of discrete onion shells, this translates into:

$$C_l(\kappa) = \frac{9H_0^4\Omega_m^2}{4c^4} \sum_j dr_j P(l/r_j, z_j) \frac{(r_s - r_j)^2}{r_s^2 a_j^2} \quad (8)$$

Fig.9 shows a comparison of the angular power spectrum in the above prediction (continuous line through the symbols) to the power spectrum directly measured from the convergence maps (symbols with errorbars). The power spectrum has been binned in adjacent multipoles with bin-width  $\Delta l = 20$ . The errorbars indicate the scatter of power within a bin. For the prediction in Eq.8 we have used the actual 3D power spectrum measured from all particles in the comoving outputs of the MICE simulation at the corresponding redshifts. The dot-dashed line uses the density in a PM grid of  $2048^3$  to estimate the same  $P(k, z)$ . In both cases, this is just an approximation because  $P(k, z)$  should be the power spectrum in the lightcone. But the difference is small because the redshift shell is quite narrow. It is also an approximation in the sense that  $P(k, z)$  in the whole box could be different to the power in a particular onion shell (redshift bin), due to sampling variance.

The measured spectrum agrees with the linear prediction on the largest scales ( $l < 100$ ), as expected. The agreement in shape and amplitude with the prediction validates the convergence maps on the largest scales. On all scales the agreement with Eq.8 is excellent, indicating that the way we have built the convergence maps is a good approximation to the true map. It also indicates that statistically, inhomogeneities in the radial direction do not affect the projection, which was assumed to get to Eq.8.

The deviations at  $l > 1000$  when using the PM grid  $P(k, z)$  (dot-dashed line) show that the power spectrum on those scales come from structure on scales smaller than the cell size used for the PM grid  $\simeq 1.5$  Mpc/h. Thus, one needs higher resolution PM simulations (or treePM algorithms for a given PM grid size) to model the larger multipoles.

In Fig.10 we show the cumulative contribution in Eq.8 from  $z = z_{min}$  to  $z = z_s$ . For multipoles  $l > 100$  the relative contributions are quite flat with 2%, 20%, 50% and 85% contribution coming for sources at  $z_{min} > 0.8$ ,  $z_{min} > 0.6$ ,  $z_{min} > 0.4$  and  $z_{min} > 0.2$ , respectively. All redshifts seem to add power in the non-linear multipoles  $l > 1000$ . Note how the lowest multipoles have a contribution  $> 50\%$  from  $z < 0.2$ , due to local structures.

### 3.2 Error comparison

The convergence map with sources at  $z_s = 1$  shown in Fig.8, nominally covers a volume,  $V_n \simeq 4/3\pi r(z_s = 1)^3 \simeq 58 \text{ Gpc}^3/\text{h}^3$  with  $r(z_s = 1) \simeq 2400 \text{ Mpc/h}$ , which is twice the volume of the parent MICE simulation,  $V_p = L_{box}^3 = (3072 \text{ Mpc/h})^3 \simeq 29 \text{ Gpc}^3/\text{h}^3$ . This is possible because we have replicated twice the box in each cartesian axis to get

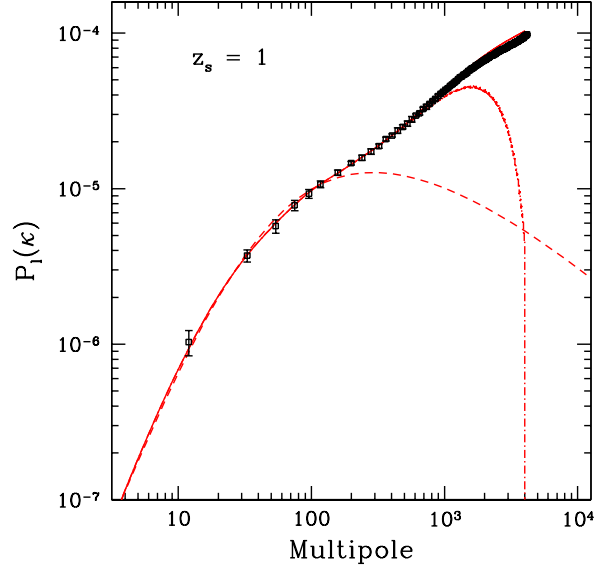


**Figure 9.** Angular power spectrum in the convergence maps (symbols with errorbars) as compared to linear theory (dashed line) and predictions from the full measured 3D power spectrum in Eq.7 (line that goes through the symbols). The dot-dashed line uses the same prediction with the 3D power spectrum measured only using a  $2048^3$  particle-mesh (PM) grid.

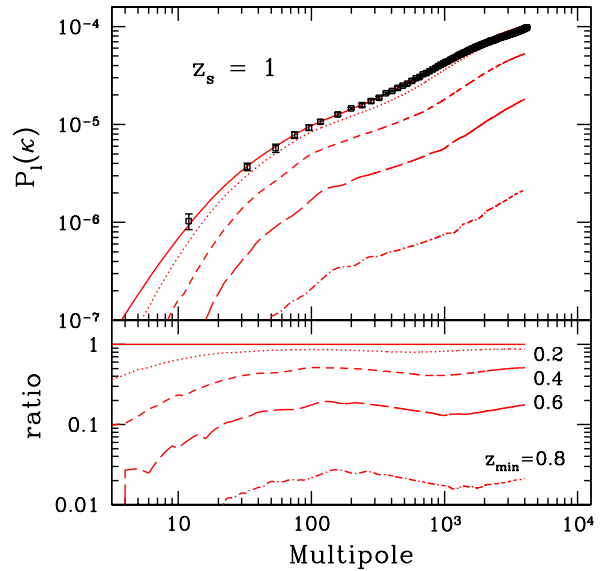


**Figure 10.** The top panel shows as dot-dashed, long-dashed, short-dashed and dotted lines the cumulative contributions to the sum in Eq.8 starting from  $z = z_{min} = 0.8, 0.6, 0.5$  and  $0.2$  respectively (as labeled in the figure) and integrated to  $z = z_s = 1$ . The bottom panel shows the ratio of these quantities to the total contribution.



to  $z \simeq 6$  (see also Section 2). However, note that to reach to  $z_s = 1$  each sky octant (1/8 of the full sky) is truly independent in the way we have built the lightcone. Firstly because each sky octant uses the same replica but with the observer placed in a different box position, so the same structures are seen differently (i.e., they are seen from a different angle and distance). Secondly, because of the shape of the lensing efficiency, the shells closer to  $z_s = 1$  (where the shell-volume is larger) give a negligible weak lensing signal. We can define an effective volume  $V_e$  sampled by the convergence map as the volume weighted by the lensing efficiency function (renormalized to be one at the peak efficiency). We find that in fact  $V_e \simeq V_n/2 \simeq 29 \text{ Gpc}^3/h^3$ . We thus conclude that the convergence map to  $z_s = 1$  samples well the full parent volume without significant repetition.

We can therefore split the sky in 10 equal area disjoint regions (a partition each 10% of the sky) and measure  $C_l$  in each of the 10 regions using a fast 2-point estimator, SpICE (Szapudi et al 2001a; Szapudi et al 2001b). We use the variance in the  $C_l$  from each region to have a direct estimate of the errors for a survey that covers a fraction  $f_{sky} = 0.1$  of the sky. We call this the “sub-sample” (SUB) error. To avoid the covariance between bins, we follow (Cabre et al 2007) and bin adjacent  $C_l$  estimations in bins of with  $\Delta l = 20$  for  $l < 100$  and  $\Delta l = 40$  for  $l > 100$ . These binwidths render the covariance matrix effectively diagonal for the binned  $C_l$ ’s (see Cabre et al 2007 for details). We can also use a variance estimator based on the rms dispersion of individual  $C_l$  amplitudes within in a given bin to estimate the error in that bin. We shall call this “intra-bin” (IB) error estimation (Fosalba & Szapudi 2004). For Gaussian distributed amplitudes this is a good estimate, because there is no correlation between adjacent multipoles.

We will compare the above errors with the traditional Gaussian estimate of the sampling variance (SV):

$$\sigma_G = C_l \sqrt{\frac{2}{f_{sky} \Delta l (2l + 1)}}. \quad (9)$$

where  $\Delta l = N_{bin}$  is the number of multipoles in each bin.

Fig.11 compares the different estimates for the relative errors in  $C_l(\kappa)$ . On scales  $l > 1000$  there is a good general agreement. SV errors seem to underestimate SUB errors by about  $\simeq 50\%$  between  $l = 500$  and  $l = 2000$ , but they yield compatible results otherwise. The IB estimator does well for  $l > 500$  but can be a up to factor of 4 too large for  $l < 500$ .

### 3.3 Power spectrum: mass resolution and shot-noise

Fig.12 shows the power spectrum in the convergence maps with different mass resolution (but same  $L_{box}$ , see Table 1). There are two different contributions to the effects shown here. One is the possible difference due to mass resolution and the other is due to the finite particle density, which results in a different shot-noise contribution.

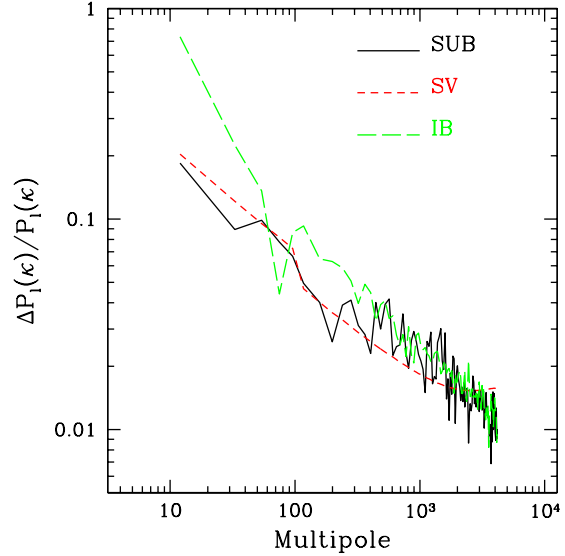


**Figure 11.** Comparison of relative errors in  $C_l(\kappa)$  for 10% of the sky: a) variance from 10 subsamples in all-sky convergence map (continuous line, SUB) b) sampling variance from Gaussian statistics (dashed line, SV) and c) intra-bin variance (long-dashed, IB).

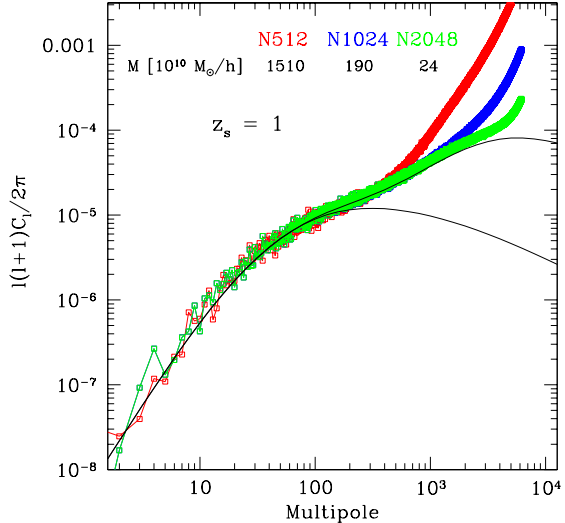


**Figure 12.** Raw power spectrum estimated from convergence maps in simulations (symbols) with  $z_s = 1$  and for different resolutions (shown in Table 1). Continuous lines show the linear and non-linear halo-fit predictions which are obtained by replacing  $P(k, z)$  in Eq.7 by the corresponding 3D power spectrum.

To correct for shot noise we subtract from the measured  $C_l$  a term given by Eq.8 with  $P(k, z) = 1/\bar{N}$ , where  $\bar{N}$  is the mean galaxy density at each redshift. The corrected spectrum is shown in Fig.13. The results for the two higher resolutions agree well up to  $l \simeq 1000$ , and roughly follow the halo-fit prescription. The power spectrum estimated from

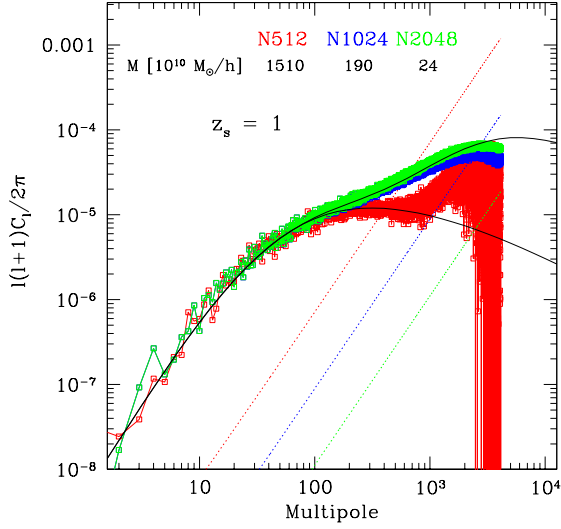


**Figure 13.** Same as Fig.12, but corrected for shot-noise. The correction in each case is shown by the dotted lines.

the low resolution map, containing  $512^3$  particles (N512) and mass resolution  $M \simeq 1.5 \times 10^{13} M_{\text{sun}}/h$ , closely follows the linear (rather than the non-linear) prediction. This could be due to the lack of small halos and it is also apparent when we compare measurements of the 3D power spectrum in outputs from the low resolution measured in the low resolution  $512^3$  MICE comoving simulations outputs to the corresponding linear  $P(k, z)$  predictions. The inability of the low resolution simulation to reproduce non-linear effects reflect the well known fact (e.g., see halo fit in Smith et al 2003) that the power on non-linear scales is dominated by the internal structure of halos with mass smaller than a few times  $10^{13} M_{\text{sun}}/h$ , i.e., comparable to the particle mass of the low resolution simulation.

### 3.4 Power spectrum: halo-fit

Fig.14 shows the relative difference between the measurements in the (all-sky) simulations and the halo-fit prediction. This prediction is obtained by using the halo-fit model  $P(k, z)$  in Eq.7. The dashed lines show the dispersion in 10 subsamples (each 10% of the sky). The halo-fit model only seems to work within 5% accuracy up to multipoles  $l < 1000$ . Deviations at smaller scales are significant (up to 30%). This is the case even for a survey which is only 10% of the sky (i.e.,  $f_{\text{sky}} = 0.1$ ), shown as dashed lines in Fig.14. Note that contrary to Fig.11 we have not binned the data here. This explains the large discrepancy between the Gaussian errors (dotted lines) and the subsample errors (short-dashed lines). Correlation between bins is strong resulting in smaller diagonal errorbars, but larger covariance for the subsample errors. Surprisingly, the Gaussian error prediction for the all-sky simulations (long dashed lines) is similar to the mea-

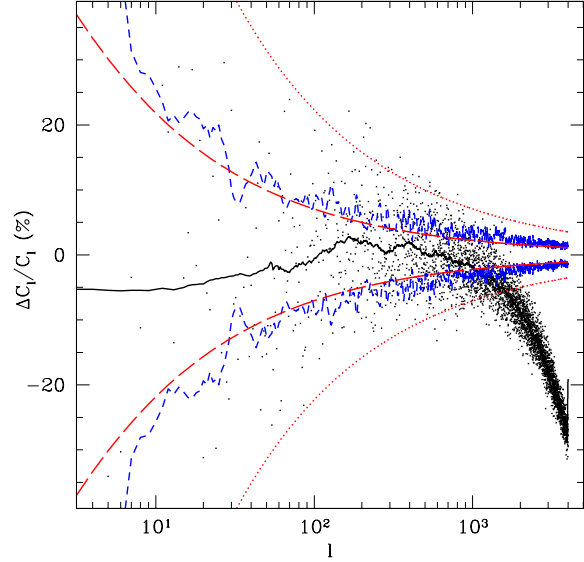


**Figure 14.** Points show the angular power spectrum of the all-sky convergence maps relative to the non-linear halo fit model. The continuous line is a smoothed version of the dots. The short-dashed line indicates the errors in 10 subsamples with 10% of the sky. The dotted (long-dashed) lines show the corresponding Gaussian error for 10% (100%) of the sky.

sured diagonal error in sub-samples of  $f_{\text{sky}} = 0.1$  (see also Cabre et al 2007 for a related discussion in cross-correlation analyses).

## 4 NON-GAUSSIANITY AND PROJECTION EFFECTS

### 4.1 Moments

It has now been well established that the  $p$ -order cumulants of the projected local density field  $\langle \kappa^p \rangle_c$  are expected to behave as

$$\langle \kappa^p \rangle_c = S_p \langle \kappa^2 \rangle_c^{p-2} \quad (10)$$

with  $p = 3, 4, \dots$ , on large scales (see Berardeau et al 2002 and references therein). The  $S_p$  parameters, quantify the departure from Gaussian behaviour, and the variance  $\langle \kappa^2 \rangle_c$  can be obtained from the power spectrum above. The measurement of the gravitational weak shear induced by the large scale structures in deep galaxy catalogs will reveal this correlation properties of the projected mass, at the level of the two-point function (Blandford et al. 1991, Miralda-Escudé, 1991, Villumsen 1996, Jain & Seljak 1996, Kaiser 1995) or for higher orders (Bernardeau, van Wearbeke & Mellier 1996, Gaztañaga & Bernardeau 1998).

Figure 15 shows the above moments for the convergence maps, smoothed with a Gaussian window of size  $\theta$ . Results are in good agreement with the analytic predictions mentioned above. More details of this comparison will be given

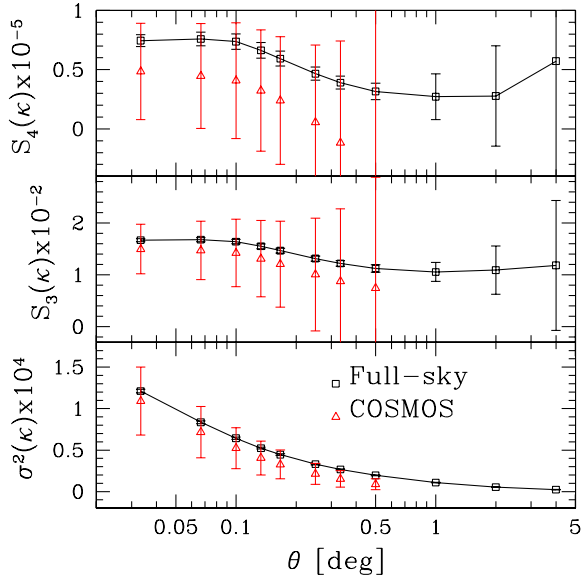


**Figure 15.** Squares show the variance (bottom), skewness (middle) and kurtosis (top) measured in the all-sky convergence map with  $z_s = 1$ . Triangles show that the mean in  $10^4$  small subsamples of 1.6 sqr.degrees that match the size of the COSMOS HST field is biased with respect to the result using all the sky. The larger errorbars represent the 1-sigma variance in the COSMOS HST subsamples. The smaller errorbars correspond to  $f_{sky} = 0.1$ .

elsewhere. Here we just want to stress that the maps are strongly non-Gaussian and we want to focus on the error estimation.

The smaller errorbars in Figure 15 correspond to  $f_{sky} = 0.1$ , while the larger errorbars correspond to a field size of 1.6 square degrees, comparable to the HST COSMOS field (Massey et al 2007). Squares correspond to the mean in the all-sky map, which agrees very well with the mean of the  $10^4$   $f_{sky} = 0.1$  subsamples. This is not the case for the mean in the  $(10^4)$  COSMOS-sized subsamples, which is severely biased. We find a 10% bias for the variance and skewness at  $2'$ , and this relative bias increases by a factor of 2 for  $10'$  and a factor of 4 for  $30'$  scales. This sampling bias is common when one has large fluctuations at the scale of the survey (eg Hui & Gaztañaga 1999), as is the case here (e.g., see also Fig.8 for a visual impression of this effect).

#### 4.2 Mass reconstruction

We could in principle use the weak lensing signal to map the 3D mass distribution in the universe (e.g., Massey et al 2007) or we can use it for the more modest task of calibrating the mass of known clusters with the idea of estimating the cluster mass function (see e.g., White, Waerbeke & Mackey 2002). Here we want to use the large statistics in our huge volume simulation to study how important projection effects could be for this mass calibration.

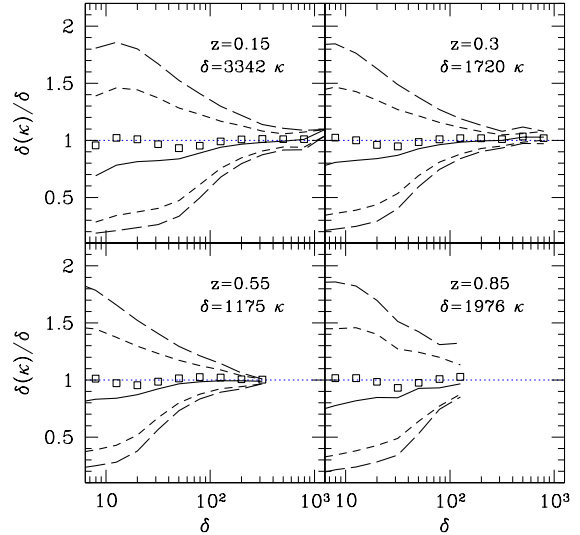


**Figure 16.** Squares show the mean ratio of reconstructed versus true density fluctuations in the convergence maps. Continuous lines represents the median of the distribution (50% percentile). The short-dashed (long-dashed) line show 25% (16%) and 75% (84%) percentiles. Each panel corresponds to a different redshift, as labeled in the plots.

At each sky pixel  $i$  we find the redshift onion shell  $j$  where the contribution to  $\kappa(i)$  in Eq.4 is maximum. This produces an array of 3D pixels  $(i, j)$  which are potential sites for large overdensities (e.g., those one can typically associate to clusters in galaxy surveys) which we want to use for mass reconstruction. We will assume that both  $j$  and  $z_s$  are known and we will use the total convergence  $\kappa(i)$  to estimate the overdensity at  $(i, j)$  as:

$$\delta(\kappa) \simeq \kappa(i) \frac{r_s a_j}{(r_s - r_j) r_j dr_j} \quad (11)$$

This procedure mimics a simple linear mass reconstruction method which assumes that the measured convergence  $\kappa(i)$  is dominated by the overdensity of pixel  $(i, j)$  (the maximum along the line-of-sight).

Square symbols in Fig.16 show the mean ratio between the reconstructed  $\delta(\kappa)$ , given by Eq.11 and the true mean fluctuation  $\delta(i, j)$  over all pixel positions  $i$  in the simulation, as a function of the true fluctuation. Each panel corresponds to a different redshift (i.e., a different value of  $j$  in Eq.11). The long-dashed lines correspond to the  $1-\sigma$  scatter in the reconstruction. As can be seen in the figure, the mean reconstruction is basically unbiased but there is quite a large scatter which increases as we decrease the size of the true fluctuation.

The top panel in Fig.17 shows cumulative histograms of the above reconstruction, where we have converted the fluctuations  $\delta$  into mass using  $M = (1 + \delta)\bar{\rho}dV$ , where  $\bar{\rho}$  is the mean pixel density and  $dV$  is the pixel volume. Note that



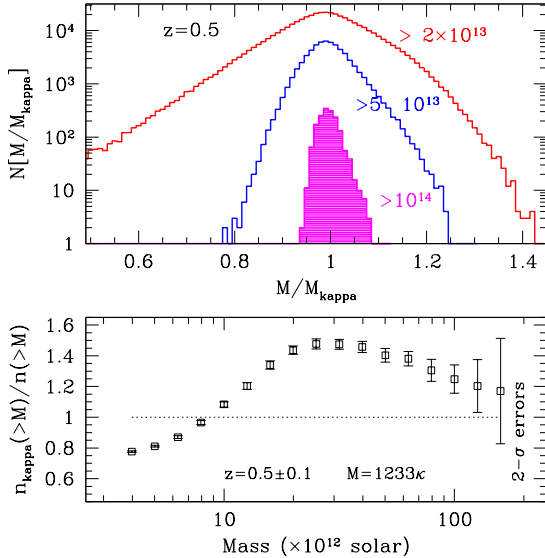


**Figure 17.** Top: Histogram showing the ratio  $M/M_{\kappa}$ , of true versus recovered convergence mass, for pixels in the simulation with true mass  $M$  above  $\times 10^{13} M_{\text{sun}}/h$  (outer histogram),  $5 \times 10^{13} M_{\text{sun}}/h$  (middle histogram) and  $10^{14} M_{\text{sun}}/h$  (inner histogram). The mean recovered mass is not biased, but the distribution is quite broad and non-Gaussian. Bottom: implication of the above histograms for the recovered mass function. The ratio of the recovered over the true cumulative number of pixels above a given mass is shown as a function of the true mass. Errorbars represent  $2\text{-}\sigma$  rms dispersion when we split the simulation in 10 pieces of  $f_{\text{sky}} = 0.1$  each.

the distribution is not Gaussian. These results agree, at least in a qualitative way, with more detailed studies over smaller simulations (e.g., White, Waerbeke & Mackey 2002).

### 4.3 Implications for the mass function

The large scatter in the above mass reconstruction has important implications for estimating the (cluster) mass function. This is illustrated by the bottom panel of Fig.17, which shows the ratio of the recovered versus the true cumulative mass function at  $z = 0.5 \pm 0.1$ . We chose this redshift because it is effectively where the convergence window function is maximum for sources at  $z_s = 1$ . We also show  $2\text{-}\sigma$  errorbars from the variance in 10 subsamples with  $f_{\text{sky}} = 0.1$ . As can be seen in the figure, there is a significant bias, given the errorbars, in the mass function. Deviations can be as large as  $\simeq 50\%$ , with an excess density at the high mass end ( $M > 10^{13} M_{\text{sun}}/h$ ) and a smaller deficit at the lower mass end. This is expected because there is a larger number density of smaller mass overdensities, which results in a greater excess of smaller mass objects that scatter into the large mass bins.

## 5 SUMMARY & CONCLUSIONS

Radial shells are a natural and convenient decomposition of the data volume to exploit large astronomical surveys. Both because of the limitations in our ability to measure precise redshifts for all objects in galaxy surveys (especially at  $z > 1$ ), and also because it is a natural way to split the survey data to study evolution or avoid redshift space distortions. Here we have presented a new generation of very large scale N-body simulations developed at the Marenostrum supercomputer using the GADGET-2 code. We have named them the *Marenostrum Institut de Ciències de l'Espai* or MICE simulations. In this first paper we have focused on a simulation that contains almost  $10^{10}$  particles in a cubical box of 3 Gpc/h on a side, what delivers good enough mass resolution ( $2.34 \times 10^{11} M_{\text{sun}}/h$ ) for studying clustering statistics of the large scale structure and cover a dynamical range of five orders of magnitude: from Gpc/h to tens of Kpc/h. This allows us to sample from the largest (linear) scales to very small (non-linear) structures.

Using this MICE simulation we have built an all-sky lightcone output that extends to high redshift by replicating the parent simulation box  $L_{\text{box}}$ . We have shown that, thanks to the way we build the lightcone, the effect of repeated structures at distances  $r > L_{\text{box}}$  from the observer is effectively negligible in clustering measurements. In order to mimic the onion-like structure of real data from galaxy surveys we have compressed the lightcone data into a set of radial shell maps of given redshift resolution. These all-sky angular maps have then been pixelized using the convenient Healpix tessellation with high spatial resolution. Our approach provides an effectively lossless method to compress simulated data by a factor  $\sim 1000$  for arcminute resolution angular maps. This allows Terabyte-sized simulations containing tens of billions of particles to be analyzed in a regular laptop.

We have presented two main applications of the onion maps for the study of large-scale structure in the universe:

- the study of BAOs in angular maps of the dark-matter distribution in the lightcone
- the construction, for the first time, of an adequate all-sky simulated weak lensing map with fine angular resolution.

The onion maps we have generated are large enough to detect the BAO scale with a precision better than 1%. We have presented the angular power spectrum of the maps (see Figs.6-7) and discussed how accurate is the Gaussian estimation of sampling errors in the presence of non-linear effects.

In Section 3, we have used the onion shells to build a new set of all-sky lensing maps. These maps are validated by comparing its power spectrum and higher orders in the map to theoretical expectations. In Fig.10 we show the relative contribution of each redshift shell to the total convergence power. Because we simulate the entire celestial sphere we can

compare theoretical prescriptions for error estimation with an error based on the rms dispersion over sky patches (sub-samples). As summarized in Fig.11, we find that Gaussian errors tend to underestimate the true errors in the power spectrum by about  $\simeq 50\%$  at non-linear scales in multipole bins between  $l = 500$  and  $l = 2000$ , even if we use broad bins to minimize covariance between adjacent multipoles. A comparison of the convergence power spectrum to the analytic halofit predictions yields discrepancies of order 30% on highly non-linear scales,  $l > 1000$  (see Fig.12-14).

We find that current lensing surveys (such as Massey et al 2007) might yield biased estimates of the clustering statistics since measurements are subject to large sampling variance. In other words, these small surveys do not represent a fair sample of the universe. This has been quantified in the variance and higher-orders of the convergence field (see Fig.15) by randomly sampling the all-sky lensing map with  $\sim 10^4$  COSMOS-sized surveys. For the variance, we estimate a  $\simeq 10\%$  bias and  $\simeq 40\%$  errors at  $2'$ , and the bias increases to 25% and 50% at  $10'$  and  $30'$  scales. We also find comparable relative biases for the skewness as a function of scale.

Our estimate of the error is significantly larger than the value reported in Massey et al (2007) for the COSMOS survey. The origin of this discrepancy might be the fact that Massey et al (2007) compute the variance using *subsamples* of the COSMOS data, and thus they do not include sample variance at the scale of the survey. Consequently, cosmological constraints on  $\sigma_8\Omega^{0.44}$  based on this estimate of the variance are expected to be also biased low significantly and the error could be underestimated by as much as a factor of 2.

We have also measured the degree of non-Gaussianity in lensing maps induced by non-linear growth. Higher order moments in the convergence field, shown in Fig.15, are compatible with theoretical expectations. In particular, they match well the amplitudes of the hierarchical scaling expected from non-linear gravitational clustering (Bernardeau et al 2002). In the case of weak lensing, these amplitudes are also strongly dependent on cosmological parameters Bernardeau, van Waerbeke & Mellier 1997; Gaztañaga & Bernardeau 1998.

Finally, we have presented a mass calibration procedure using lensing maps. In Fig.17 we illustrate how well we expect to recover mass estimates based on all-sky convergence maps. Upcoming wide surveys, such as DES (Annis et al 2005), plan to calibrate the cluster mass function using the weak lensing information. We have shown here that this approach is a promising tool for calibrating masses, but it needs to be corrected from systematic biases that arise because of the large scatter induced by projection effects. Further work needs to be done to check the impact of these considerations in specific mass calibration methods, such as the one recently presented in Johnston et al. 2007.

Note added in proof: after our paper was submitted, other papers appeared presenting applications of N-body simulations for CMB lensing analyses (Das & Bode 2008; Carbone et al. 2008). We note that the method introduced in our paper can be straightforwardly applied to CMB lensing. We will present this application elsewhere.

## ACKNOWLEDGMENTS

We would like to thank Anna Cabré, Carlton Baugh, Francis Bernardeau, Manuel Delfino, Gus Evrard, and Volker Springel, for useful discussions at different stages of this work. Special thanks for Santi Serrano for his help with visualization tools for the MICE simulations and Fig.1 of this paper. We acknowledge support from the MareNostrum supercomputer (BSC-CNS, [www.bsc.es](http://www.bsc.es)) and Port d'Informació Científica (PIC, [www.pic.es](http://www.pic.es)) where the original simulations were run and stored, the Spanish Ministerio de Ciencia y Tecnología (MEC), project AYA2006-06341 with EC-FEDER funding and research project 2005SGR00728 from Generalitat de Catalunya. Some of the plots in this paper were produced using CMBview, developed by Jamie Portsmouth ([www.jportsmouth.com/code/CMBview/cmbview.html](http://www.jportsmouth.com/code/CMBview/cmbview.html)). PF acknowledges support from the Spanish MEC through a Ramon y Cajal fellowship. EG would also like to thank the hospitality of Instituto Nacional de Astrofísica, Óptica y Electrónica (INAOE, Mexico), Galileo Galilei Institute for Theoretical Physics (Florence, Italy) and the Center for Cosmology and Particle Physics (NYU, USA). MM acknowledges support from the DURSI department of the Generalitat de Catalunya and the European Social Fund. This work was supported by the European Commission's ALFA-II programme through its funding of the Latin-American European Network for Astrophysics and Cosmology (LENAC).

## REFERENCES

- Adelman-McCarthy et. al., (The SDSS Collaboration), 2006 *Astrophys J. Supp* 162, 38-48
- Annis, J., et al. (Dark Energy Survey white paper) 2005, *astro-ph/0510195*
- Angulo, R.E., Baugh, C.M., Frenk, C.S., Lacey, C.G., 2008, *MNRAS*, 383, 755
- Bacon D. J., Refregier A., Clowe D., Ellis R. S., 2001, *MNRAS*, 325, 1065
- Bartelmann, M & Schneider, P., 2001, *Phys.Rept.* 340, 291
- Bernardeau, F., Waerbeke, L. van & Mellier, Y. 1997, *A&A*, 322, 1
- Bernardeau, F., van Waerbeke, L., Mellier, Y., 1997 *A&A* 322, p1-18
- Bernardeau, F., Colombi, S., Gaztañaga, E., Scoccimarro, R., 2002, *Phys. Rept.* 367, 1
- Blandford R. D., Saust A. B., Brainerd T. G., Villumsen J. V., 1991, *MNRAS* 251, 600
- Blaizot J., Wadadekar Y., Guiderdoni B., Colombi S. T., Bertin E., Bouchet F. R., Devriendt J. E. G., Hatton S., 2005, *MNRAS*, 360, 159

- Bond, J.R., Kofman, L., Pogosyan, D., 1996, *Nature*, 380, 603
- Cabre, A., Fosalba, P., Gaztañaga, E., Manera, M., 2007, *MNRAS*, 381, 1347
- Carbone C., Springel V., Baccigalupi C., Bartelmann M., Matarrese S., 2008, *MNRAS*, 814
- Cooray, A. & Hu, W., 2002, *ApJ*, 574, 19
- Das S., Bode P., 2008, *ApJ*, 682, 1
- Evrard, A.E., et al, 2002, *ApJ*, 573, 7
- Forero-Romero J. E., Blaizot J., Devriendt J., van Waerbeke L., Guiderdoni B., 2007, *MNRAS*, 379, 1507
- Fosalba, P. & Szapudi, I., 2004, *ApJ* 617, L95
- Gaztañaga, E. & Bernardeau, F., 1998, *A&A* 331, 829
- Górski, K. M., Hivon, E., & Wandelt, B. D. 1999, in *Proc. MPA-ESO Conf., Evolution of Large-Scale Structure: From Recombination to Garching*, p.37, Ed. A.J.Banday, R.K.Seth, & L.A.N. da Costa (Enschede: PrintPartners Ipskamp)
- Hui L., Gaztañaga E., 1999, *ApJ*, 519, 622
- Jain, B. & Seljak, U. 1997, *ApJ*, 484, 560
- Jain, B., Seljak, U. & S.White 2000, *ApJ*, 530, 547
- Jarvis M., Jain B., Bernstein G., Dolney D., 2006, *ApJ*, 644, 71
- Johnston, D.E., et al., 2007, *arXiv:0709.1159*
- Kaiser N., 1995, *ApJ*, 439, 1
- Kitzbichler M. G., White S. D. M., 2007, *MNRAS*, 376, 2
- Miralda-Escude J., 1991, *ApJ* 380, 1
- Massey, R., et al 2007, *Nature*, 4445, 286
- Massey, R., et al 2007, *ApJS* in press, *astro-ph/0701480*
- Refregier, A., Rhodes, J., & Groth, E., 2002, *ApJ* 572, L131
- Refregier A., 2003, *ARA&A*, 41, 645
- Scoccimarro R., Zaldarriaga, M., & Hui, L., *ApJ*, 527, 1
- Semboloni, E. et al, 2007, *MNRAS*, 375, L6
- Smith, R.E. et al 2003, *MNRAS*, 341, 1311
- Springel, V., 2005, *MNRAS*, 364, 1105
- Springel, V. et al 2005, *Nature*, 435, 639
- Szapudi, I., 2001, *ApJ* 548, L115
- Szapudi, I., Prunet, S., & Colombi, S., 2001, *ApJ*, 561, L11
- Vale, C. & White, M., 2003, *ApJ*, 592, 699
- Villumsen, J V 1996, *MNRAS*, 281, 369
- Waerbeke L. van et al. 2001, *MNRAS*, 322, 918
- Wambsganss, J. Cen, R. & Ostriker, J., P., 1998, *ApJ*, 494, 29
- White, M. & Hu, W., 2000, *ApJ*, 537, 1
- White, M., Waerbeke, L. van & Mackey, J., 2002, *ApJ*, 575, 640
- White, M. & Vale, C., 2004, *Astrophys. J.*, 22, 19